Title
Nanosheet-assembled MoSe 2 and S-doped MoSe 2−x nanostructures for superior lithium storage properties and hydrogen evolution reactions

Journal
Inorganic Chemistry Frontiers, 2(10)

ISSN
2052-1545

Authors
Yang, Yong
Wang, Shitong
Zhang, Jingchao
et al.

Publication Date
2015

DOI
10.1039/c5qi00126a

Peer reviewed

Volume 2 | Number 10 | October 2015

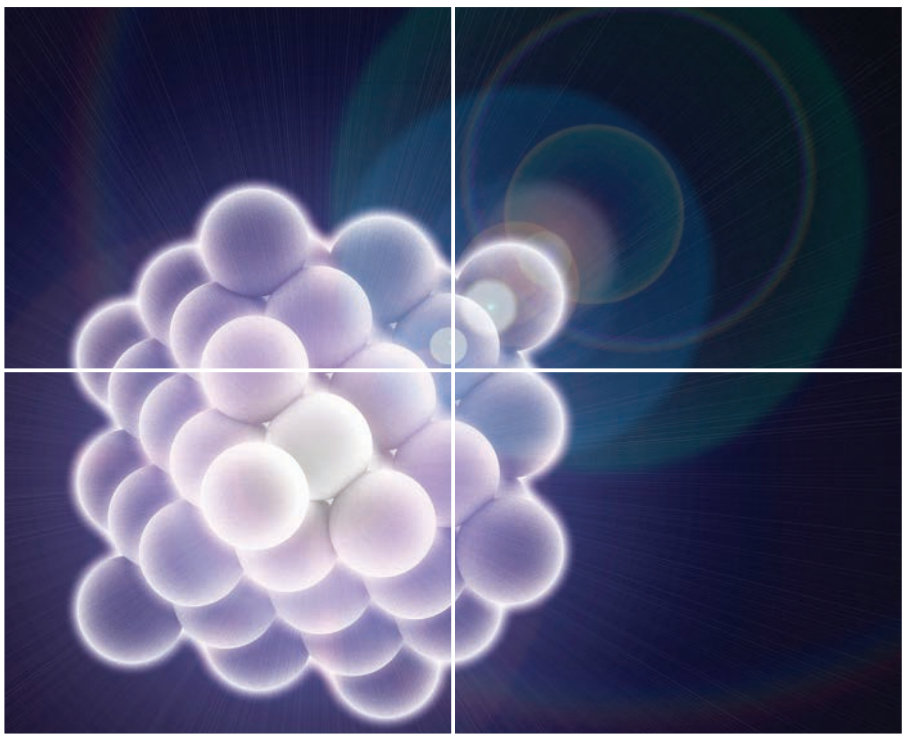

INORGANIC CHEMISTRY

FRONTIERS

Chinese Chemical Society

ROYAL SOCIETY OF CHEMISTRY

http://rsc.li/frontiers-inorganic

INORGANIC CHEMISTRY
FRONTIERS

RESEARCH ARTICLE

Cite this: *Inorg. Chem. Front.*, 2015, **2**, 931

Nanosheet-assembled $MoSe_2$ and S-doped $MoSe_{2-x}$ nanostructures for superior lithium storage properties and hydrogen evolution reactions†

Yong Yang, Shitong Wang, Jingchao Zhang, Haoyi Li, Zilong Tang and Xun Wang*

Received 20th July 2015,
Accepted 21st August 2015

DOI: 10.1039/c5qi00126a

rsc.li/frontiers-inorganic

The development of layered molybdenum chalcogenides with largely exposed active sites is receiving intense interest because of their potential applications in energy storage and catalysis. Here, we report a strategy for the synthesis of hierarchical $MoSe_2$ and S-doped $MoSe_{2-x}$ nanostructures resulting from the assembly of nanosheets. The incorporation of S exposes a large quantity of the active edge sites as well as abundant unsaturated sites. For example, the hierarchical S-doped $MoSe_{2-x}$ nanotubes show a high reversible capacity and excellent cycling performance as an anode material for lithium-ion batteries (LIB). In addition, the synthesized S-doped $MoSe_{2-x}$ nanosheets exhibit excellent catalytic activity and superior stability for the hydrogen evolution reaction (HER) in acidic medium. The excellent performance of S-doped $MoSe_{2-x}$ nanosheets has been attributed to the synergistic effect of the high density of active sites as well as the enhanced conductivity.

Introduction

Layer-structured transition-metal dichalcogenides (TMDs), such as $MoSe_2$ and MoS_2, have drawn great attention because of their interesting physical and chemical properties and wide potential applications in energy storage,[1] electronics,[2] optoelectronics,[3] and catalysis.[4] Particularly, two-dimensional (2D) and monolayered TMDs with exposed edges were demonstrated to be very promising electrocatalysts for the HER in recent years.[5] However, these 2D nanosheets tend to restack and condense, which compromises their performance in many practical applications.[6] It has been suggested that self-assembly is considered to be one of the most efficient methods to maintain the advantages of the individual nanosheets.[7] As a consequence, assembling these 2D nanosheet building blocks into three-dimensional (3D) hierarchical architectures to maximize the number of edge sites and large specific surface area still remains a significant challenge.

$MoSe_2$, as a typical layered TMDs semiconducting material, consists of Se–Mo–Se sandwich layers by weak van der Waals interactions.[8] Both computational and experimental results showed that catalytically active sites stem from the exposed planes on the edges rather than on the basal surfaces of nanosheets.[9] Besides, the high electrical conductivity of catalysts leads to faster reaction kinetics and electrocatalytic activity.[10] Recently, intense efforts have been devoted to increasing the density of the active sites and electrical conductivity.[11] Yan reported highly active ultrathin S-doped $MoSe_2$ nanosheets for efficient electrochemical hydrogen evolution.[12] Cui and coworkers synthesized vertically aligned $MoSe_2$ nanofilms on carbon fiber paper to maximally expose the active edges on the paper surface. The HER activity of $MoSe_2$ had been further improved by Ni doping.[13] Li prepared ultrathin $MoS_{2(1-x)}Se_{2x}$ alloy nanoflakes and found that the alloy nanostructures showed more active HER performance than either pure MoS_2 or $MoSe_2$.[14] These results suggest that anion-doping/substitution can be used as an effective strategy to promote the catalytic performance and to improve the electrical conductivity.

We herein report a facile bottom-up solution method to synthesize hierarchical $MoSe_2$ and S-doped $MoSe_{2-x}$ nanostructures resulting from the assembly of nanosheets. An interesting structural evolution from nanocaterpillars to nanosheets was observed by S-doping. The incorporation of S not only leads to a large quantity of exposed active sites, but also generates abundant unsaturated sites. Owing to the unique mesoporous tubular structure , the obtained S-doped $MoSe_{2-x}$ nanotubes showed a high reversible capacity and excellent cycling performance as an anode material for LIB. What is more, the resulting S-doped $MoSe_{2-x}$ nanosheets possessed enhanced HER catalysis with a low onset overpotential of ~95 mV and a Tafel slope of 68 mV per decade, compared

Tsinghua University, Beijing, China. E-mail: wangxun@mail.tsinghua.edu.cn
†Electronic supplementary information (ESI) available. See DOI: 10.1039/c5qi00126a

with $MoSe_2$ nanocaterpillars and S-doped $MoSe_{2-x}$ nanotubes. The enhanced catalytic activity of S-doped $MoSe_{2-x}$ nanosheets has been attributed to the synergistic effect of the high density of active sites as well as the enhanced electrical conductivity.

Experimental section

Chemicals

All chemicals were purchased from Sinopharm Chemical Reagent Beijing Company and were used as received without further purification. Deionized water was used throughout the experiment.

Preparation of $MoSe_2$ nanocaterpillars. In the synthesis of hierarchical $MoSe_2$ nanostructures, selenium powder and ammonium molybdate are used as the Se and Mo sources, respectively. A mixture of Se powder (0.76 mmol) and ammonium molybdate $[(NH)_6Mo_7O_{24}{\cdot}4H_2O]$ (0.05 mmol) was added to 15 mL of octylamine and 12 mL of oleyl alcohol in a 40 mL Teflon-lined autoclave under intense stirring. The sealed vessel was placed in an oven and heated at 200 °C for 12 h. After cooling, the black product was washed with alcohol several times and finally dried at 60 °C by vacuum drying.

Preparation of S-doped $MoSe_{2-x}$ nanosheets. In a typical synthesis, a mixture of S powder (0.32 mmol), Se powder (0.76 mmol) and ammonium molybdate $[(NH)_6Mo_7O_{24}{\cdot}4H_2O]$ (0.064 mmol) was added to 15 mL of octylamine and 12 mL of oleyl ethanol while other conditions are kept constant. The sealed vessel was placed in an oven and heated at 200 °C for 12 h. After cooling, the black product was washed and finally dried at 60 °C by vacuum drying.

Preparation of S-doped $MoSe_{2-x}$ nanotubes. In a typical synthesis, a mixture of S powder (1.08 mmol), Se powder (1.27 mmol) and ammonium molybdate $[(NH)_6Mo_7O_{24}{\cdot}4H_2O]$ (0.075 mmol) was added to 15 mL of octylamine and 12 mL of ethanol in a 40 mL Teflon-lined autoclave under intense stirring. The sealed vessel was placed in an oven and heated at 200 °C for 12 h. After cooling, the black product was washed and finally dried at 60 °C by vacuum drying. For preparation of MoS_2, MoS_2 was synthesized through the same process as that of S-doped $MoSe_{2-x}$ nanotubes except without adding Se powder. All nanosheet-assembled samples were transferred to a quartz glass tube. The tube was then placed in a heating furnace and purged with Ar. The sample was calcined at 500 °C for 2 h, with a heating rate of 3 °C min^{-1}.

Characterization

X-ray diffraction (XRD) characterization was carried on a Rigaku D/max-2400 X-ray diffractometer using CuK radiation (λ = 1.5418 Å) ranging from 10° to 80° at 40 kV voltage and a 40 mA current. The morphologies and structures of the samples were determined by a HITACHI H-7700 TEM with an accelerating voltage of 100 kV, and a FEI Tecnai G2 F20 S-Twin high-resolution (HR) TEM equipped with an energy dispersive spectrometer (EDS) analysed at 200 kV. The scanning electron microscopy (SEM) was performed on a LEO 1530. Nitrogen adsorption/desorption measurements were conducted on a Quadrasorb SI-MP instrument. X-ray photoelectron spectroscopy (XPS) experiments were conducted on scanning X-ray microprobe (Quantera SXM, ULVAC-PHI. INC) operated at 250 kV, 55 eV with monochromated Al Kα radiation.

Lithium ion battery measurements

The working electrodes were prepared by mixing the samples, conductive carbon black (Super-P), and poly (vinyldifluoride) (PVDF) at a weight ratio of 75 : 15 : 10 and pasted on a pure copper foil. The slurry was uniformly pasted onto the Cu foil with a blade. The electrodes were dried at 120 °C in a vacuum oven for 12 h to remove the solvent before pressing. Cell assembly was carried out in an Ar-filled glove box with moisture and oxygen concentrations below 1.0 ppm, using lithium metal as the counter electrode. The electrolyte is 1 M $LiPF_6$ in a mixture of ethylene carbonate and diethyl carbonate (1 : 1 by weight). The cycling and rate performances were recorded on a LAND celltest 2001A system with a voltage of 0.01–3 V *vs.* Li^+/Li.

Electrochemical measurements

The electrochemical measurements were conducted using an electrochemical workstation (CHI660E) in a typical three-electrode setup with an electrolyte solution of 0.5 M H_2SO_4, Pt plates as the counter electrode, and a saturated calomel electrode (SCE) as the reference electrode. Typically, 5 mg of catalyst and 50 μL of Nafion solution (5 wt%) were dispersed in 1 mL water–ethanol solution (1 : 3) by sonicating for 1 h to form a homogeneous ink. Then 10 μL of catalyst ink was loaded onto a glassy carbon electrode of 5 mm diameter (loading ~0.25 mg cm^{-2}). Linear sweep voltammetry (LS) was conducted in 0.5 M H_2SO_4 with a scan rate of 5 mV s^{-1}. Prior to measurement, a resistance test was made and the iR compensation was applied by using the CHI software. Electrochemical impedance spectroscopy (EIS) measurements were also carried out in the frequency range of 100 kHz–0.1 Hz using a Princeton PARSTAT P4000 AMETEK Co. Ltd electrochemistry workstation. In all measurements, the SCE reference electrode was calibrated with respect to reversible hydrogen electrode (RHE). RHE calibration was performed experimentally according to the reported method. In 0.5 M H_2SO_4, E(RHE) = E(SCE) + 0.281 V.

Results and discussion

In the synthesis of the hierarchical $MoSe_2$ nanostructure, selenium powder and ammonium molybdate are used as the Se and Mo resources, respectively. The morphology of the sample is initially characterized using scanning electron microscopy (SEM) and transmission electron microscopy (TEM) at different magnifications. It is obvious to see that the products exhibit worm-like shape with a diameter of about 300 nm and a length of several micrometers (Fig. 1a, b and S1†). As can be clearly seen from Fig. 1c, the obtained sample is composed of numerous curled $MoSe_2$ layers. Fig. 1e shows the typical high-resolution TEM (HRTEM) image taken from the selected area

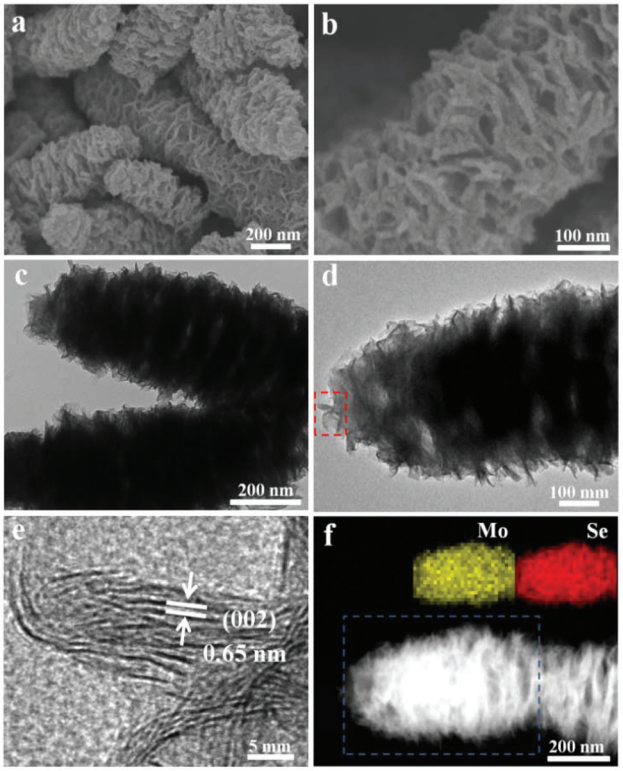

Fig. 1 (a and b) SEM images of the as-prepared $MoSe_2$ nanocaterpillars. (c and d) TEM and HRTEM images of $MoSe_2$ nanocaterpillars. (e) HRTEM analysis taken from the selected areas marked by rectangles in (d). (f) HAADF-STEM image of the $MoSe_2$ nanostructure. The insets are the corresponding EDS mapping images, which show that molybdenum and selenium are homogeneously distributed throughout the whole nanostructure.

marked in Fig. 1d. The obvious lamellar structures with an interlayer spacing of 0.65 nm are observed, indicating the nature of the layered structure. The HRTEM image in Fig. S2† shows that the interplanar distance between the lattice fringes is 0.28 nm, which is consistent with the (100) plane of the hexagonal $MoSe_2$ phase. In addition, the selected area electron diffraction (SAED) pattern with concentric diffraction rings represents the polycrystalline structure of the sample (inset in Fig. S2†). The high-angle annular dark-field scanning TEM (HAADF-STEM) and the corresponding energy-dispersive X-ray (EDX) mapping (Fig. 1f and S3†) show the uniform distribution of molybdenum and selenium throughout the structure.

X-ray diffraction (XRD) was carried out to identify the crystallographic structure, as shown in Fig. S3.† Compared with the standard values, all of the broad diffraction peaks indicate the nanoscale structure and the peaks are shifted to the left side. The obvious (002) diffraction can be attributed to the well-stacked nanosheets. X-ray photoelectron spectroscopy (XPS) was used to further investigate the chemical states of Mo and Se in the products (Fig. S4†). The peaks at 228.7 eV and 231.9 eV results from the Mo $3d_{5/2}$ and Mo $3d_{3/2}$, respectively, whereas the peak at 55.1 eV represents the binding energies of Se 3d. The Mo 3d and Se 3d spectra indicate that the valence states of elements Mo and Se are +4 and −2,[15] respectively. In order to further improve the structure, Raman spectroscopy was carried out, as shown in Fig. S5.† The characteristic A_{1g} and E^1_{2g} Raman modes located at 236 cm^{-1} and 280 cm^{-1} represent the out-of-plane mode and in-plane mode of $MoSe_2$, which confirmed the composition of the products as $MoSe_2$.[5c] The corresponding ion coupled plasma atomic emission spectrometry (ICP-AES) also shows that the atomic ratio of Mo : Se is about 1 : 2.1. These results demonstrate that nanosheet-assembled $MoSe_2$ nanostructures have been successfully prepared through this facile solvothermal method.

Sulfur powder was directly added into this amine–oleyl ethanol solution, and the S-doped $MoSe_{2-x}$ nanosheets can thus be obtained. Fig. S6a† shows the XRD pattern of S-doped $MoSe_{2-x}$ nanosheets. Compared with the $MoSe_2$, it is interesting to note that the (002) peak of the S-doped $MoSe_{2-x}$ nanosheets is diminished. In addition, the diffraction peaks at $2\theta = 56.6°$ is shifted to higher angles compared to that of pure $MoSe_2$ (Fig. S6b†). Such a right shift of peaks can be ascribed to the smaller ionic radius of S.[10] As shown in Fig. 2a, the morphology of the sample changes into a three dimensional network stemming from the disorderly assembly of nanosheets. HRTEM observation clearly reveals the formation of nanosheets with ripple structures and a large quantity of exposed edge sites of the (002) plane. The thicknesses of the nanosheets are measured to be in the range of 0.65–2.6 nm with a thickness of 2–5 atomic layers (Fig. 2b and d). What is more, the spacings between adjacent (002) planes were

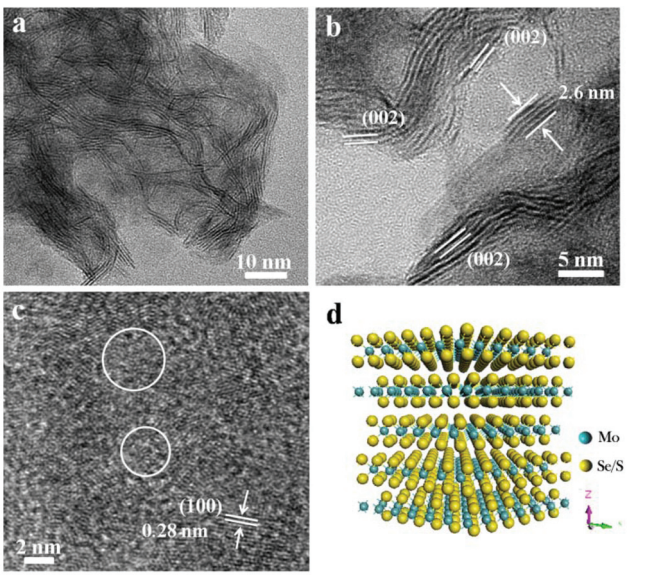

Fig. 2 (a) TEM image of as-prepared S-doped $MoSe_{2-x}$ nanosheets. (b) HRTEM image of the folded edge of the stacking nanosheets with different atomic layers. (c) HRTEM image of the basal plane of the nanosheet, indicating the existence of nanodomains with random atomic arrangements. (d) The corresponding atomic stacking models in (b). Thicknesses of the curled edges are measured to be 2.6 nm.

measured ranging from 6.5 Å to 7.5 Å (Fig. S7†). The curvature of the edge of the (002) plane is attributed to the introduction of S, which tends to expose more basal planes as terminating surfaces. The STEM-EDX mapping image (Fig. S7c†) indicates the incorporation of S into the nanosheets and the uniform distribution of Mo and Se. The ICP-AES analysis also indicates that the atomic ratio of Mo : Se is 1 : 1.55, suggesting Mo-rich with a lot of Se vacancies. It is believed that this unsaturated structure results in the formation of more active edge sites. In addition, the HRTEM image in Fig. 2c shows the existence of nanodomains with polycrystalline structures in the basal plane. The nanodomains will provide additional structural defects in their basal planes because of the addition of S. Therefore, these defect-rich S-doped $MoSe_{2-x}$ nanosheets possess many active unsaturated Se atoms and active sites along the basal edges, which is advantageous for electrocatalytic applications.

It is worth noting that ultralong nanotubes can be obtained in large quantities by increasing the amount of sulfur in the amine–ethanol system. The SEM images (Fig. 3a and S8†) show that the obtained nanotubes are highly uniform with a diameter of about 200–300 nm and a length of 4–5 μm. A representative SEM is shown in Fig. 3b. This cross-sectional image shows that the samples possess a well-defined tubular void structure with a pore size of 50 nm. The hierarchical structure was further characterized by TEM (Fig. 3c and d), which shows that the obtained nanotubes are also constructed by flexible sheet-like subunits. The HRTEM images in Fig. 3e and S8† show that these visible curled edges assembled by disordered nanosheets measure about 0.7 nm. The EDS elemental mapping shows that the elements S, Se and Mo are uniformly distributed throughout the nanotubes (Fig. 3f and S9†) and the ratio of Se : S is about 1.1 : 1 (Table S1†). The XRD analysis (Fig. S6†) shows the crystal structure of the S-doped $MoSe_{2-x}$ nanotubes. Note that increasing the sulfur content results in a continuous right shift for the diffraction (110) peaks, indicating the compaction of unit cells. The dotted lines in Fig. S6b† are added to facilitate in tracking the shifting of the (110) peak. This result is in agreement with the previous reports.[14] In order to better investigate the chemical states of S-doped $MoSe_{2-x}$ nanotubes, XPS analysis was carried out. As shown in Fig. S10,† two characteristic peaks located at 229.1 eV and 232.4 eV can be assigned to Mo $3d_{5/2}$ and Mo $3d_{3/2}$, respectively.[14,15,21a] The binding energies of Se 3d5/2 and Se 3d3/2 are 54.6 eV and 55.2 eV. And the minor peaks at 162.1 eV and 163.4 eV correspond to the binding energies of S $2p_{3/2}$ and $2p_{1/2}$, suggesting the presence of Mo–S bonding.[12]

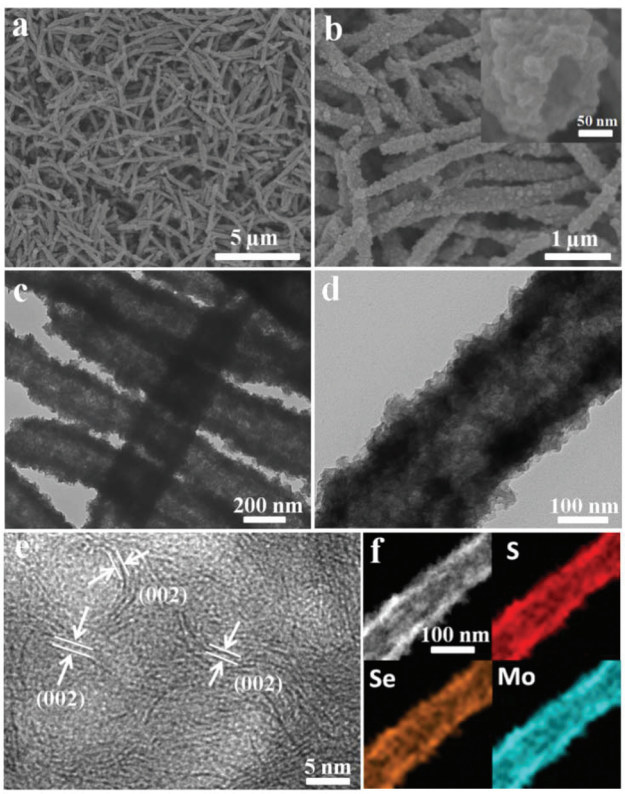

Fig. 3 (a and b) SEM images of as-prepared S-doped $MoSe_{2-x}$ nanotubes. The inset in b represents a typical tubular structure. (c–e) TEM and HRTEM images of S-doped $MoSe_{2-x}$ nanotubes. (f) HAADF-STEM image and the corresponding EDS mapping images, indicating that sulphur, molybdenum and selenium are distributed throughout the whole nanostructure.

It should be emphasized that alcohols are critical to form sheet-assembled architecture for amine-based synthetic systems. It has been found experimentally that the assemblies depend on the dipole–dipole interactions for primary crystal nuclei, and as a result affect the interaction between nuclei and determine the initial assembly.[16,17] The function of various alcohols was investigated in detail, For example, microspheres and irregular structure can be obtained using heptanol and ethanol while other conditions are kept constant (Fig. S11†). In such synthesis systems, oleyl alcohol serves not only as the solvent, but also as a surfactant to limit the growth of the basal plane. Only a microsized structure was obtained without oleyl alcohol (Fig. S11a†). With S-doping, the morphology of $MoSe_2$ changed from nanocaterpillars to nanosheets. In addition, the incorporation of S results in a large quantity of exposed active sites and generates abundant unsaturated sites in their basal planes.

In view of the hollow structure and the ultrathin nanosheet-assembled feature, nitrogen adsorption–desorption isotherms and pore size distribution measurements were carried out to investigate the permanent porosity of the samples. The Brunauer–Emmett–Teller (BET) surface area (Fig. S12†) of the S-doped $MoSe_{2-x}$ nanotubes is 49.8 $m^2\ g^{-1}$ (Langmuir surface area, 72.4 $m^2\ g^{-1}$). The corresponding pore size distribution is about 30 nm and 4 nm. The latter is likely associated with the channels resulting from the assembly of the nanosheets. In addition, BET specific surface area of $MoSe_2$ nanocaterpillars and S-doped $MoSe_{2-x}$ nanosheets are 13.3 $m^2\ g^{-1}$ and 23.0 $m^2\ g^{-1}$, respectively (Fig. S12c and d†). In order to get rid of the residual oleylamine and expose more active sites of the samples, the as-synthesized samples were heated at 500 °C under an Ar atmosphere. After annealing, the tubular mor-

phology is still well retained (Fig. S13†), indicating excellent structural stability. Given that these sheet-assembled structures have large quantities of exposed edge sites, the as-prepared samples could be useful in energy storage and electrocatalytic hydrogen evolution.

To demonstrate the advantages of these sheet-assembled assemblies, we first evaluated their lithium storage properties as anode materials for LIBs. Fig. 4a and c show the first three discharge/charge profiles of the $MoSe_2$ nanocaterpillars, S-doped $MoSe_{2-x}$ nanotubes, and the S-doped $MoSe_{2-x}$ nanosheet electrode at a current rate of 100 mA g^{-1} between 0.01 and 3.00 V *versus* Li^+/Li. These electrodes display similar electrochemical storage characteristics, which is very similar to those of the metal dichalcogenides.[18] For the S-doped $MoSe_{2-x}$ nanotubes, there are two notable voltage plateaus in the discharge–charge curves at around 0.9 V and 1.5 V, respectively, indicating the lithium insertion/de-insertion process. The corresponding CV curves of S-doped $MoSe_{2-x}$ nanotubes during the first three cycles are presented in Fig. S14a.† The reduction peak at ~0.8 V during the first cycle may be attributed to the formation of $LiMoS_xSe_{2-x}$, and the other peak at ~0.3 V corresponds to the conversion reaction process. These peaks disappear in the subsequent cycles with the appearance of new peaks at ~1.7 V, which is similar to the previous metal dichalcogenide results.[18] The initial discharge capacity of the S-doped $MoSe_{2-x}$ nanotubes and S-doped $MoSe_{2-x}$ nanosheets electrode is 1316 and 1400 mA h g^{-1}, which is superior to the theoretical capacity of $MoSe_2$.[18] The high initial lithium discharge capacity might be attributed to the nanosheet-assembled nanoarchitecture with a porous structure, which is a common phenomenon for the nanostructured anode material. A large electrode–electrolyte contact area and shortened solid-state diffusion paths for both electronic and ionic transfer allow the material to achieve a high lithium–ion intercalation capability. The obvious irreversible capacity for all samples in the initial cycle is ascribed to the formation of a solid electrolyte interface layer. As shown in Fig. 4d, the cycling performance of the above three sample electrodes between 0.01 and 3.00 V were compared. Owing to the unique tubular structure, S-doped $MoSe_2$ nanotubes exhibited the highest reversible capacity of 947 mA h g^{-1} in the 30th cycle and the corresponding coulombic efficiency is maintained at about 95%. Note that the capability of S-doped $MoSe_{2-x}$ nanotubes is superior to those metal dichalcogenide anode results previously reported.[19,20] By contrast, the capacities of the $MoSe_2$ nanocaterpillars and S-doped $MoSe_{2-x}$ nanosheets decrease dramatically after 30 cycles. Moreover, S-doped $MoSe_2$ nanotubes also exhibit excellent rate capability at different current densities, as shown in Fig. S15.† When the discharge/charge rate increases from 50 to 500 mA g^{-1}, the capacity decreases from 1054 to 1020, 982, and 667 mA h g^{-1}. Moreover, the capacity can restore to about 1000 mA h g^{-1} when the current changes into 100 mA g^{-1}. The outstanding energy storage performance of the S-doped $MoSe_{2-x}$ nanotubes could probably be summarized from several aspects. Firstly, the hollow architecture not only can facilitate the penetration of the electrolyte in the electrode, but also can buffer the stress caused by the volume excursions in charging and discharging reactions (Fig. S16†). Furthermore, the S-doped $MoSe_{2-x}$ mesoporous nanotubes may benefit the transport of Li^+ ions, resulting in the enhanced Li storage property.

The HER catalytic activity of the samples were further evaluated in 0.5 M H_2SO_4 solution using a rotating disc electrode (RDE) in a typical three-electrode setup on a glassy carbon electrode. Fig. 5a shows the polarization curves of the samples

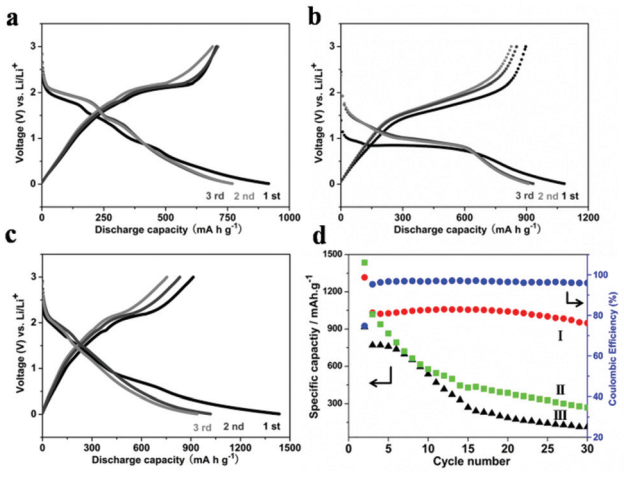

Fig. 4 Discharge–charge curves of different samples for the 1st, 2nd, and 3rd cycles. (a) $MoSe_2$ nanocaterpillars; (b) S-doped $MoSe_{2-x}$ nanotubes. (c). S-doped $MoSe_{2-x}$ nanosheets. (d) Specific discharge capacity of S-doped $MoSe_{2-x}$ nanotubes (I), S-doped $MoSe_{2-x}$ nanosheets (II), $MoSe_2$ nanocaterpillars (III) and the coulombic efficiency of S-doped $MoSe_2$ nanotubes. The tests are conducted at a current density of 100 mA g^{-1} between 0.01 and 3.0 V *vs.* Li/Li^+.

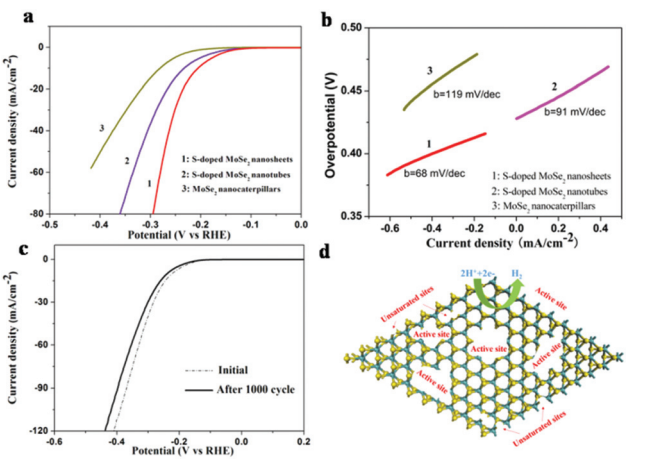

Fig. 5 (a) Polarization curves of $MoSe_2$ nanocaterpillars, S-doped $MoSe_{2-x}$ nanosheets and S-doped $MoSe_{2-x}$ nanotubes; and (b) the corresponding Tafel plots; (c) Durability test for the S-doped $MoSe_{2-x}$ nanosheets after 1000 CV cycles. (d) Schematic illustration of the unsaturated edges on the nanosheet (100) basal plane and edge-rich ultrathin nanosheets for HER.

measured with a scan rate of 2 mV s^{-1}. The polarization curves of S-doped $MoSe_{2-x}$ nanosheets exhibit high activity with a small overpotential of ~95 mV. And the overpotential is as small as 235 mV *vs.* RHE at a HER current of 20 mA cm^{-2}, while the S-doped $MoSe_2$ nanotubes and $MoSe_2$ nanocaterpillars exhibited comparatively poor HRE activity with 266 mV and 318 mV, respectively. Therefore, S-doped $MoSe_2$ nanosheets are more superior in catalytic activity than $MoSe_2$ nanocaterpillars and S-doped $MoSe_2$ nanotubes. It can be inferred that S-doped $MoSe_2$ nanosheets with large quantities of exposed edge sites lead to a higher current at low overpotential.

The Tafel slopes were further investigated for the intrinsic activity of all samples. The linear portions of the Tafel plots (Fig. 5b) were fit to the Tafel equation ($\eta = b \log j + a$)[21] yielding Tafel slopes of 68, 91, 119 mV per decade for S-doped $MoSe_{2-x}$ nanosheets, S-doped $MoSe_{2-x}$ nanotubes and $MoSe_2$ nanocaterpillars, respectively. The small Tafel slope usually means that the hydrogen generation rate increases faster with increasing overpotential. Such a small Tafel slope of 68 mV per decade means that the rate-limiting step of the S-doped $MoSe_{2-x}$ nanosheets was the electrochemical desorption and the Volmer–Heyrovsky mechanism.[22] In addition, the electrical conductivity of samples can be increased by S-doping, which is confirmed by electrochemical impedance spectroscopy (EIS) analysis, as shown in Fig. S17.† The semicircle indicates the charge transfer resistance (R_{ct}) of H^+ reduction.[23] The S-doped $MoSe_2$ nanosheets exhibited much lower charge transfer impedance of 176 Ω than S-doped $MoSe_{2-x}$ nanotubes (234.2 Ω) and $MoSe_2$ nanocaterpillars (800 Ω), which is consistent with the polarization measurements. The reduced impedance will provide faster electron transfer and facilitate the kinetics of the HER. The stability of the S-doped $MoSe_{2-x}$ nanosheets was evaluated by cycling the electrode at a scan rate of 100 mV s^{-1}. As shown in Fig. 5c, the performance of the S-doped $MoSe_2$ nanosheets after 1000 cycles showed only slight degradation compared with the fresh electrode, indicating a good cycling performance. This loss may be attributed to the consumption of H^+ in the solution or the remaining H_2 bubbles on the surface of the electrode that hinder the reaction.[11a,24] The existence of unsaturated Se atoms and edge-rich ultrathin nanosheets are active sites for proton adsorption (Fig. 5d). Therefore, a high density of active sites and the good electrical conductivity of S-doped $MoSe_2$ nanosheets are responsible for the high catalytic performance.

Conclusions

In summary, we report a facile solvothermal method to prepare hierarchical $MoSe_2$ nanocaterpillars and S-doped $MoSe_{2-x}$ nanostructures. An interesting structural evolution from nanocaterpillars to nanosheets was observed by S-doping. When evaluated as an anode material for LIB, the as-synthesized S-doped $MoSe_{2-x}$ nanotubes manifested a high specific capacity and good cycling performance because of the unique tubular structure, which is much better than that of the synthesized $MoSe_2$ nanocaterpillars and S-doped $MoSe_{2-x}$ nanosheets. Besides, the resulting S-doped $MoSe_{2-x}$ nanosheets are rich in both unsaturated Se atoms as well as active sites along the basal edges, which exhibit high HER catalytic activity and good stability. Such a high performance has been attributed to the synergistic effect of the high density of active sites as well as the enhanced conductivity. The present work suggests that the catalytic performance can be enhanced by anion doping. Significantly, this effective strategy might be extended to design other $MoSe_2$-based materials for high-performance HER catalysis and other applications.

Acknowledgements

This work was supported by NSFC (91127040, 21221062), and the State Key Project of Fundamental Research for Nanoscience and Nanotechnology (2011CB932402).

References

1 X. Zhang and Y. Xie, *Chem. Soc. Rev.*, 2013, **42**, 8187–8199.
2 L. Jia, X. Sun, Y. Jiang, S. Yu and C. Wang, *Adv. Funct. Mater.*, 2015, **25**, 1814–1820.
3 (*a*) L. Zhang, H. B. Wu, Y. Yan, X. Wang and X. W. Lou, *Energy Environ. Sci.*, 2014, **7**, 3302–3306; (*b*) F. Zhou, S. Xin, H. W. Liang, L. T. Song and S. H. Yu, *Angew. Chem., Int. Ed.*, 2014, **53**, 11552–11556.
4 S. Zhuo, Y. Xu, W. Zhao, J. Zhang and B. Zhang, *Angew. Chem., Int. Ed.*, 2013, **52**, 8602–8606.
5 (*a*) H. Vrubel, D. Merki and X. Hu, *Energy Environ. Sci.*, 2012, **5**, 6136–6144; (*b*) H. I. Karunadasa, E. Montalvo, Y. Sun, M. Majda, J. R. Long and C. J. Chang, *Science*, 2012, **335**, 698–702; (*c*) L. P. Jia, X. Sun, Y. M. Jiang, S. J. Yu and C. M. Wang, *Adv. Funct. Mater.*, 2015, **25**, 1814–1820.
6 M. Chhowalla, H. S. Shin, G. Eda, L. J. Li, K. P. Loh and H. Zhang, *Nat. Chem.*, 2013, **5**, 263–275.
7 M. Xu, T. Liang, M. Shi and H. Chen, *Chem. Rev.*, 2013, **113**, 3766–3798.
8 (*a*) D. Sun, S. Feng, M. Terrones and R. E. Schaak, *Chem. Mater.*, 2015, **27**, 3167–3175; (*b*) Y. N. Ko, S. H. Choi, S. B. Park and Y. C. Kang, *Nanoscale*, 2014, **6**, 10511–10515.
9 J. Xie, H. Zhang, S. Li, R. Wang, X. Sun, M. Zhou, J. Zhou, X. W. Lou and Y. Xie, *Adv. Mater.*, 2013, **25**, 5807–5813.
10 H. Tang, K. Dou, C. Kaun, Q. Kuang and S. Yang, *J. Mater. Chem. A*, 2014, **2**, 360–364.
11 (*a*) X. Zhou, J. Jiang, T. Ding, J. Zhang, B. Pan, J. Zuo and Q. Yang, *Nanoscale*, 2014, **6**, 11046–11051; (*b*) Z. H. Deng, L. Li, W. Ding, K. Xiong and Z. D. Wei, *Chem. Commun.*, 2015, **51**, 1893–1896; (*c*) Y. Jiang, X. Li, S. Yu, L. Jia, X. Zhao and C. Wang, *Adv. Funct. Mater.*, 2015, **25**, 2693–2700; (*d*) D. Merki, H. Vrubel, L. Rovelli, S. Fierro and X. Hu, *Chem. Sci.*, 2012, **3**, 2515–2525.
12 C. Xu, S. J. Peng, C. L. Tan, H. X. Ang, H. T. Tan, H. Zhang and Q. Y. Yan, *J. Mater. Chem. A*, 2014, **2**, 360–364.

13 (*a*) H. Wang, D. Kong, P. Johanes, J. J. Cha, G. Zheng, K. Yan, N. Liu and Y. Cui, *Nano Lett.*, 2013, **13**, 3426–3433; (*b*) H. Wang, C. Tsai, D. Kong, K. Chan, F. Abild-Pedersen, J. K. Nørskov and Y. Cui, *Nano Res.*, 2015, **8**, 566–575; (*c*) D. Kong, H. Wang, J. J. Cha, M. Pasta, K. J. Koski, J. Yao and Y. Cui, *Nano Lett.*, 2013, **13**, 1341–1347.

14 Q. Gong, L. Cheng, C. Liu, M. Zhang, Q. Feng, H. Ye, M. Zeng, L. Xie, Z. Liu and Y. Li, *ACS Catal.*, 2015, **5**, 2213–2219.

15 H. Tang, K. Dou, C. Kaun, Q. Kuang and S. Yang, *J. Mater. Chem. A*, 2014, **2**, 360–364.

16 P. Wang, Y. Yang, J. Zhuang and X. Wang, *J. Am. Chem. Soc.*, 2013, **135**, 6834–6837.

17 P. Wang, H. Sun, Y. Ji, W. Li and X. Wang, *Adv. Mater.*, 2014, **26**, 964–969.

18 (*a*) Y. Shi, C. Hua, B. Li, X. Fang, C. Yao, Y. Zhang, Y. Hu, Z. Wang, L. Chen, D. Zhao and G. D. Stucky, *Adv. Funct. Mater.*, 2013, **23**, 1832–1838; (*b*) C. Zhu, X. Mu, P. A. van Aken, Y. Yu and J. Maier, *Angew. Chem., Int. Ed.*, 2014, **53**, 2152–2156; (*c*) X. H. Cao, Y. M. Shi, W. H. Shi, H. Rui, Q. Y. Yan, J. Kong and H. Zhang, *Small*, 2013, **47**, 3433–3438.

19 (*a*) K. Chang and W. X. Chen, *Chem. Commun.*, 2011, **47**, 4252–4254; (*b*) S. K. Park, S. H. Yu, S. Woo, J. Ha, J. Shin, Y. E. Sung and Y. Piao, *CrystEngComm*, 2012, **14**, 8323–8325; (*c*) S. J. Ding, D. Y. Zhang, J. S. Chen and X. W. Lou, *Nanoscale*, 2012, **4**, 95–98.

20 (*a*) K. Chang and W. X. Chen, *ACS Nano*, 2011, **5**, 4720–4728; (*b*) S. K. Park, S. H. Yu, S. Woo, B. Quan, D. C. Lee, M. K. Kim, Y. E. Sung and Y. Piao, *Dalton Trans.*, 2013, **42**, 2399–2405.

21 (*a*) H. Vrubel, D. Merki and X. Hu, *Energy Environ. Sci.*, 2012, **5**, 6136–6144; (*b*) Y. Li, H. Wang, L. Xie, Y. Liang, G. Hong and H. Dai, *J. Am. Chem. Soc.*, 2011, **133**, 7296–7299.

22 Y. Yan, B. Xia, X. Ge, Z. Liu, J. Wang and X. Wang, *ACS Appl. Mater. Interfaces*, 2013, **5**, 12794–12798.

23 (*a*) B. E. Conway and B. V. Tilak, *Electrochim. Acta*, 2002, **47**, 3571–3594; (*b*) B. Qu, X. B. Yu, Y. J. Chen, C. L. Zhu, C. Y. Li, Z. X. Yin and X. T. Zhang, *ACS Appl. Mater. Interfaces*, 2015, **7**, 14170–14175.

24 J. Xie, J. Zhang, S. Li, F. Grote, X. Zhang, H. Zhang, R. Wang, Y. Lei, B. Pan and Y. Xie, *J. Am. Chem. Soc.*, 2013, **135**, 17881–17888.